Catalysis Letters (2019) 149:1565–1578
https://doi.org/10.1007/s10562-019-02757-z

Active TiO_2-Nanostructured Surfaces for CO Oxidation on Rh Model Catalysts at Low-Temperature

R. Camposeco[1] · S. Castillo[2] · M. Hinojosa-Reyes[3] · R. Zanella[1] · Julio C. López-Curiel[4] · Gustavo A. Fuentes[4] · Isidro Mejía-Centeno[2]

Received: 11 October 2018 / Accepted: 22 March 2019 / Published online: 3 April 2019

Abstract

We investigated the CO oxidation at low temperature over Rh (1 wt%) supported on TiO_2-nanotubes and nanoparticles. We found that tri-titanic acid phase of the nanotubes promotes the interaction between Ti^{4+} and Rh^{3+} to reduce Rh^{3+} to Rh^{1+} and Rh^{+1} to Rh^0, compared to the anatase phase. In fact, as the Rh^0/Ti^{4+} ratio increases, CO and OH adsorption increases and CO oxidation light-off shifts to lower temperature, from 120 to 60 °C. We found that there is a redox equilibrium between $Rh^0 + Ti^{4+}$ and $Rh^{\delta+} + Ti^{3+}$ ($\delta < 3$). However, the Rh^0/Ti^{4+} ratio, hence redox equilibrium, seems to be limited by the valence band energy of the catalysts. We concluded that there is a strong electronic metal-support interaction between nanotubes of TiO_2 and Rh-nanoparticles that promotes the catalytic performance. Therefore, the valence band is a major factor determining the catalytic activity.

Graphical Abstract

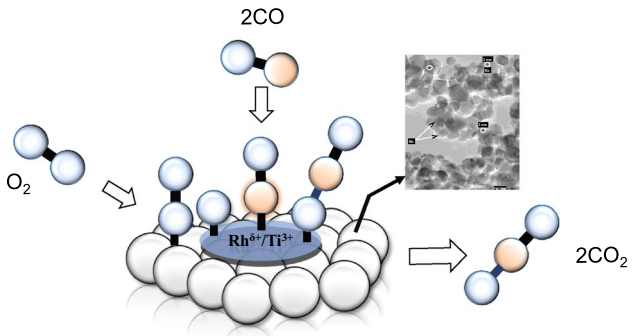

$Rh^0 + Ti^{4+} \leftrightarrow Rh^{\delta+} + Ti^{3+}$ ($\delta<3$)

Keywords CO oxidation · Rhodium · TiO_2 nanotubes · TiO_2 nanoparticles · Deactivation

✉ Isidro Mejía-Centeno
imejia@imp.mx

1 Instituto de Ciencias Aplicadas y Tecnología, Universidad Nacional Autónoma de México, 04510 México City, México

2 Dirección de Investigación en Transformación de Hidrocarburos, Instituto Mexicano del Petróleo, 07730 México City, México

3 Facultad de Ciencias, Universidad Autónoma de San Luis Potosí, 78000 San Luis Potosí, SLP, México

4 Departamento de Ingeniería de Procesos, Universidad A. Metropolitana-Iztapalapa, 09340 México City, México

1 Introduction

The oxidation of CO over metal surfaces is probably one of the most studied catalytic reactions for developing emission control technologies for vehicles and stationary sources [1–4]. Platinum, palladium, gold, and rhodium dispersed on a reducible metal oxide supports (as Fe_2O_3, Co_3O_4, CeO_2, MgO, TiO_2), become active for the low-temperature oxidation of CO, even at room temperature [5–9]. The catalytic activity for CO oxidation depends on several parameters

such as the catalyst deposition method, the metal-support interface interaction, and pretreatment of the catalyst [9]. Besides, the structure and chemical composition of the support are also relevant. TiO_2, for instance, is exceptionally active for low-temperature oxidation of CO [10].

On Au/TiO_2 and Pd/TiO_2 supported catalysts, CO oxidation is structure sensitive and the reaction proceeds via the interaction between weakly bonded CO and oxygen located at the defect centers [9, 10]. The particle size of gold seems to have a major impact when compared to the effects due to the support [11]. In the case of crystals of Ru, Joo et al. [12] reported that the catalytic activity for CO oxidation increases as the size of the Ru nanoparticles increased (from 2 to 7 nm). The formation of a Ru oxide on the larger nanoparticles with a higher stability respect to that formed on the smaller particles explains their results [12].

CO oxidation over Rh dispersed on SiO_2, Al_2O_3 and TiO_2 was reported by Ioannides et al. [13]. They reported that the maximum turn over frequency (TOF) is approximately the same for the three catalysts [13]. However, Rh/SiO_2 presented an oscillatory behavior, a phenomenon not observed over Rh/Al_2O_3 and Rh/TiO_2 catalysts. They proposed [13] that oxidation/reduction of the Rh surface was the dominant mechanism responsible of the oscillatory behavior. However, the support affects the particle size distribution [14]. Crystalline Rh was observed on Rh/SiO_2, while dispersed clusters were observed on Rh/Al_2O_3 and Rh/TiO_2 [14]. In fact, adsorption and desorption of CO was not dissociative on Rh/SiO_2, whereas CO dissociation was reported on Rh/Al_2O_3 and Rh/TiO_2 [14]. On single crystals, McClure and Goodman [15] reported that catalytic CO oxidation on Pt-group metals (Rh, Pt, Pd and Ru) follows Langmuir–Hinshelwood kinetics. They also reported that the most active surface of the Pt-group metals is one with minimal CO coverage [15]. Tauster et al. [16] reported that the reduction of noble metals at low temperature (200 °C) produces well dispersed metals, which have the capacity to adsorb CO. However, when the reduction of the same materials was performed at high temperature (500 °C), the adsorption of CO decreases almost to zero. They reported [16] that the change in adsorption capacity is not due to metal agglomeration. In fact, the chemical interaction between the metal and the support affects the chemisorption properties of the noble metals.

Use of an alternate support, as titanate nanotubes, gives the possibility to achieve a high loading of active metal with a high dispersion [17]. Besides, the morphology of the nanotubes (mesoporous), the high surface area, and the absence of micropores enhances the transport of the molecules to the active sites during reaction. Furthermore, in redox reactions the semiconducting properties of the titanate nanotubes result in a strong electronic interaction between the support and the catalyst, improving the catalytic performance [17]. The electronic metal-support interactions (EMSI) involve the correlation between the electronic properties of catalytic sites and catalytic activity [18–20]. EMSI results from the contact between highly dispersed metal particles and reducible oxides [18]. The alteration of the chemical properties of metal sites results from the perturbations in their electronic properties via bonding interaction with the support [19]. In the case of CO oxidation on Cu/CeO_2, for instance, it has been reported [20] that copper-ceria interactions are involved with the formation of the Cu^+ active species via a redox equilibrium $Ce^{4+} + Cu^+ \leftrightarrow Ce^{3+} + Cu^{2+}$. The reducibility and oxygen exchange of ceria is associated with the O vacancies. In the case of Cu/CeO_2 catalysts, Lykaki et al. [21] reported that the particle size and morphology play an important role on the structural/redox properties on binary oxides. The ceria morphology rather than structural/textural properties affects the reducibility and oxygen mobility [21]. In fact, the oxygen mobility affects the copper-ceria interactions of the Ce^{4+}/Ce^{3+} and Cu^{2+}/Cu^+ redox equilibrium. Lykaki et al. [21] reported 100% for CO conversion at 100 °C on Cu/CeO_2-NR catalyst.

In this line, our research group [22] has also reported a high CO conversion (100%) at 300 °C on titanate nanotubes. Méndez-Cruz et al. [23] reported 100% of CO conversion at 190 °C on titanate nanotubes calcined at 400 °C. However, with the addition of 3 wt% of gold nanoparticles to the nanotubes (with a pretreatment of the support at 400 °C and the catalyst at 300 °C) they reported 100% of CO conversion at 150 °C. During the thermal annealing process, however, there is transformation from nanotubes to anatase that is enhanced by the presence of Rh nanoparticles [24].

Catalytic oxidation of CO at low temperature is currently an important area of research. In spite of the extensive reports in this field, however, more investigation is still required in order to propose new catalytic materials, which would ultimately help to improve the air quality of urban settings. In this work, we report for a first time the catalytic CO oxidation over Rh catalysts supported on commercial TiO_2 (1Rh/P25), titanate nanotubes (obtained by the hydrothermal method, 1Rh/NTSG), titanate nanotubes with 3 wt% of alumina (1Rh/NTSG-Al_2O_3), and TiO_2 obtained by the sol–gel method (1Rh/TSG). The main objective of this work was to investigate the effect of the supports over Rh particle size distribution, their redox properties and a possible correlation with the catalytic activity during the CO oxidation reaction.

2 Experimental

2.1 Synthesis of TiO_2 (TSG)

TiO_2-nanocrystals, labeled as TSG, were prepared by the sol–gel method. 36.6 mL of titanium (IV) isopropoxide (Aldrich, 97%) were dissolved in 145 mL of 2-propanol

(Baker, 99.9%). The solution was set under constant stirring and then HNO_3 was added to adjust the reaction medium pH at 3. By adding bidistilled water to the system, the hydrolysis was accomplished. The solution was maintained under constant stirring and reflux until the gel was formed. The gel was dried at 80 °C for 12 h and then calcined at 400 °C for 4 h. The support was labelled as TSG.

2.2 Synthesis of the Titanate Nanotubes (NTSG)

Titanate nanotubes, labeled as NTSG, were prepared by hydrothermal treatment. 1.5 g of the TSG support synthesized from the sol–gel method and 60 mL of aqueous NaOH (10 N) were mixed in a Parr reactor at 140 °C for 24 h at 200 rpm. The solution was filtered, and the slurry was washed with a solution of HCl up to reach a pH of 3. The solid was washed with deionized water up to reach a pH of 7. The material was dried under vacuum at 80 °C for 12 h and calcined in air at 400 °C for 4 h.

2.3 Synthesis of the Titanate Nanotubes with Alumina (NTSG-3Al_2O_3)

Titanate nanotubes with alumina were prepared by the hydrothermal method. 3.0 g of TSG containing 3 wt% of Al_2O_3 were dissolved in 60 mL of a NaOH aqueous solution (10 N). The solution was mixed in an autoclave Parr reactor at 140 °C for 24 h. The autoclave was set at 200 rpm. Thereafter, the solution was filtered, and the slurry was washed with HCl up to reach a pH close to 3. The solid was washed with deionized water up to reach a pH value close to 7. Finally, the material was dried under vacuum at 80 °C for 12 h, and then calcined in air at 400 °C for 4 h. The sample was labeled as NTSG-3Al_2O_3.

2.4 Deposition of Rhodium

The supports TSG, P25 (from Degussa), NTSG and NTSG-3Al_2O_3 were added to a solution (120 mL) of water containing rhodium (III) nitrate hydrate. Rhodium was adjusted to obtain catalysts with 1 wt%. The catalysts were dried at 80 °C for 12 h and then calcined at 400 °C for 4 h. The catalysts were labeled as 1Rh/P25, 1Rh/TSG, 1Rh/NTSG and 1Rh/NTSG-3Al_2O_3.

2.5 Catalytic Tests

Samples of 50 mg of catalyst were tested in a tubular quartz reactor mounted on a temperature-programmed electronic furnace (Chromalox 2104). A porous quartz frit disk was placed in the middle of the tube to support the catalyst. Before the activity measurements, the catalysts were activated in situ, first, with a flow of 50 mL/min of H_2/He at 300 °C for 4 h. New samples of catalysts (50 mg) were activated in situ, second, with a flow of air (50 mL/min) at 300 °C for 4 h. The catalysts then were cooled down up to − 5 °C under the same flow of gas. The synthetic mixture of gases containing 1 vol.% of CO and 1 vol.% of O_2 was introduced to the system of reaction with a total flow of 100 mL/min. The gas balance was N_2. The heating rate was 2 °C/min, from − 5 to 200 °C.

The gases were analyzed on-line by a GC (Agilent Technologies 6890 N) equipped with a FID detector and a methanizer (HP Plot Q column). The stability of the catalysts as a function of the time was analyzed at 100 °C during 16 h using 50 mg of catalyst activated in situ, under the reaction conditions described above.

2.6 Characterization

The X-ray diffraction (XRD) patterns were recorded at room temperature with Cu Kα radiation (1.5404 Å) in a Bruker Advance D-8 diffractometer having a theta–theta configuration and a graphite secondary-beam monochromator. The data were collected for scattering angles (2θ) ranging from 4 to 80° with a step of 0.02° for 2 s per point. High resolution transmission electron microscopy (HRTEM) analyses of the samples were performed with a JEOL 2200FS microscope operating at 200 kV and equipped with a Schottky-type field emission gun and an ultrahigh resolution pole piece (Cs = 0.5 mm, point-to-point resolution, 0.190 nm). The samples were ground, suspended in isopropanol at room temperature and dispersed by ultrasonic agitation. An aliquot of the solution was dropped on a 3-mm-diameter lacey carbon copper grid.

Scanning transmission electron microscopy (STEM) was obtained by using a high-angle annular dark field (HAADF) detector, which collects electrons that undergo Rutherford scattering; therefore, elements with high Z show higher intensities and a white contrast in the image. The textural properties were obtained by means of an ASAP-2000 analyzer from Micrometrics. The specific surface area was calculated from the Brunauer–Emmett–Teller (BET) equation from N_2 physisorption at 77 K. The pore size distribution was obtained by the Barrett–Joyner–Halenda (BJH) method from the desorption branch.

Infrared (IR) spectra were obtained using a Nicolet-8700 Fourier transform-infrared. FTIR spectra were obtained with a vacuum chamber Spectra Tech DRIFTs equipment. These spectra were registered after accumulating 50 scans at a resolution of 4 $cm^{-1}$with nitrogen flow at 10 cm^3/min. The nitrogen flow was maintained during the measurements (25 °C to 500 °C). The H_2-TPR study of the catalysts was performed in a RIG-150 unit under a flow of 10% H_2/Ar gas mixture (30 mL/min). The heating

rate was of 10 °C min from room temperature to 600 °C. H_2O produced during the reduction process was trapped before the TCD detector.

Dispersion is defined as the surface Rh atoms divided by total Rh atoms in the catalyst [24]. The mean particle size of Rh was calculated by supposing they are hemispherical in shape, by Eq. (1):

$$D_p = \frac{6M}{D\rho\sigma N_A} \quad (1)$$

where M is the molecular weight of Rh (102.91 g/mol), D is the Rh fractional dispersion, ρ is the Rh metal density (12.4 g/cm^3), σ is the area occupied by a surface Rh atom (7.58 A^2/atom), and N_A is the Avogadro constant [24]. We assume that the chemisorption stoichiometry is H:Rh = 1 [24].

X-ray photoelectron spectroscopy (XPS) was performed with a Thermo VG Scientific Escalab 250 spectrometer equipped with a hemispherical electron analyzer and an Al Kα radiation source (1486.6 eV) powered at 20 kV and 30 mA, respectively. The binding energy (BE) was determined by using carbon C (1 s) line as reference with a binding energy of 284.6 eV. The powdered samples were pressed into a disk and placed on a sample holder in a vacuum chamber. The spectrometer was operated at a pass-energy of 23.5 eV, and the base pressure in the analyzing chamber was maintained in the order of 3×10^{-8} mbar. Peak fitting was done by using XPSPEAK 41 with Shirley background. A Thermo Scientific Evolution 600 UV–vis spectrometer was used to record directly the diffuse reflectance spectra between 200 and 800 nm (using the reflectance spectra as a reference) at room temperature.

2.7 Band Gap Energy, Valence Band, and Conduction Band

The band gap energy (Eg) was estimated from the UV–vis spectra [25]. The Kubelka–Munk function F(R) was plotted versus $h\upsilon$ (h is the Planck´s constant, Js, υ is the light frequency, 1/s). The band gap energy (eV) was estimated from the linear fit of the flat section from the UV–vis spectrum. In fact, the Eg value was estimated by extrapolating the slope to F(R) = 0. The valence band (VB) energy was estimated from the XPS valence band spectrum [26]. The VB values were estimated by extrapolating the slope to the base-line. The conduction band (CB) energy can be estimated from the Eg and VB (Eg = CB − VB).

3 Results and Discussion

3.1 Catalytic Tests and Deactivation

Figure 1a presents the conversion of CO as a function of the temperature on 1Rh/P25, 1Rh/NTSG-3Al_2O_3, 1Rh/TSG and 1Rh/NTSG catalysts. CO oxidation starts at 60 °C on 1Rh/P25 catalyst and its conversion increases with temperature

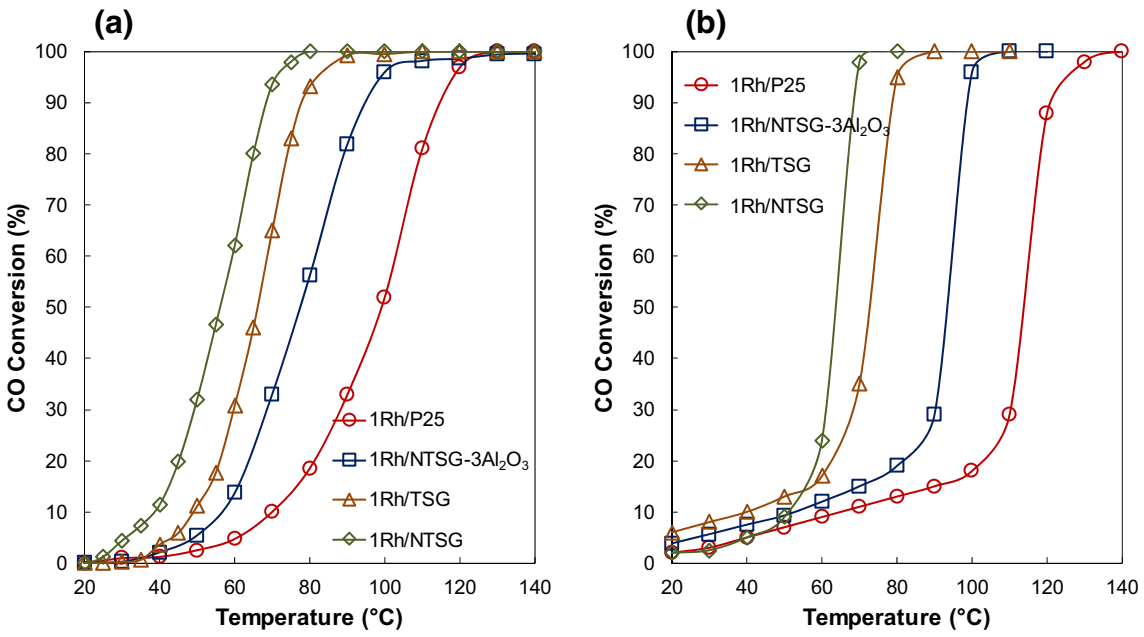

Fig. 1 CO oxidation as a function of the temperature over several catalysts. **a** Pre-reduced catalysts at 300 °C for 4 h under H_2/He (50 mL/min). **b** Pre-oxidized catalysts at 300 °C for 4 h under air (50 mL/min). 1 vol.% of CO, 1 vol.% of O_2, 50 mg of catalyst, and total flow of 100 mL/min

until reaching 100% at about 130 °C. The four catalysts show a similar behavior for the CO oxidation. However, CO oxidation light-off and 100% conversion shift to lower temperature when compared with 1Rh/P25. For the 1Rh/NTSG-Al_2O_3 catalyst, the complete conversion of CO was reached at 110 °C, and 90 °C for the 1Rh/TSG catalyst. The best catalyst to remove CO at low temperature, under our reaction conditions, was 1Rh/NTSG. This catalyst (1Rh/NTSG) starts the CO oxidation at 25 °C. At 75 °C, CO conversion was 98%, and 100% at 80 °C. CO conversion on pre-oxidized catalysts, presented in Fig. 1b, follows the trend observed on pre-reduced catalysts. However, the complete CO conversion occurs at even lower temperature on pre-oxidized catalysts.

Table 1 presents some of the structural characteristics of the catalysts used in this work. The Rh surface density (Rh atoms/nm^2), defined as the number of rhodium atoms per square nanometer of the catalyst; was calculated from the Rh content and the BET surface area as follows [27]:

$$Rh\ surface\ density = \frac{Rh\ percentage \times 6.023 \times 10^{23}}{surface\ area \times 102.9 \times 10^{18}} \quad (2)$$

The Rh surface density provides a convenient parameter for comparing catalysts prepared on supports with a wide range of surface areas [27]. Rh dispersion was obtained by Eq. (1). We found that there is not a clear correlation among CO conversion, surface area, and Rh surface density. However, the catalytic activity seems to correlate with the Rh dispersion and Rh particle size. We found that as the particle size diminishes, the dispersion increases, and the CO conversion shifts to lower temperature. In fact, our results show that 1Rh/NTSG catalyst presents the highest dispersion (88%), the lowest particle size (0.5 nm) and the best catalytic activity (100% at 80 °C) when compared to the other catalysts. Note that as the procedure for the addition of Rh was the same for the four catalysts, Rh dispersion and the particle size depend on the support.

Commercial TiO_2 (P25 as support) presents a particle size between 25 and 35 nm. In this case, Rh reached 45% of dispersion with a support particle size around 3.5 nm. However, on nanoparticles of TiO_2 obtained by the sol–gel method (TSG) with a crystal size around 9 nm, the Rh dispersion was 73%, with a particle size of Rh around 1.0 nm. Furthermore, the support composed by titanate nanotubes (NTSG) improved the Rh dispersion up to 88% with a particle size around 0.5 nm, but the addition of 3 wt% of Al_2O_3 to the titanate nanotubes (NTSG-3Al_2O_3) hindered the Rh dispersion, which only reached 40% with a particle size around 3.0 nm, slightly above of that reported for P25 (37%). We suggest then that titanate nanotubes, as support, promote the Rh dispersion by decreasing their particle size when compared with supports composed by nanoparticles of TiO_2. However, the addition of Al_2O_3 to the titanate nanotubes (despite their high surface area, 182 m^2/g) has a detrimental effect on the dispersion and particle size, and, in consequence, upon catalytic activity.

It is interesting to observe in Table 1 that the band gap energy (Eg) of the supports is affected by the Rh dispersion and particle size. The P25 and NTSG-3Al_2O_3 supports present a band gap energy of 3.18 and 3.29 eV, respectively. For these materials (P25 and NTSG-3Al_2O_3), the Rh dispersion is very close, between 37 and 40%. For the TSG support, Eg is 3.12 eV and 3.00 eV for the NTSG support. As the particle size decreases and the Rh dispersion increases, Eg attains a lower value. It is not clear how the band gap energy of the support correlates with the CO oxidation.

There are some indications that the electronic metal-support interactions effect [19, 20], may play a role on CO oxidation, as it is affected by the Rh dispersion, Rh particle size as well as by Rh oxidation state. Khodakov et al. [27], in a study on the effects of support on the structure and catalytic behavior of supported vanadia, reported that at a given value of surface density, the characteristics of the support influences the apparent dispersion and absorption edge energy

Table 1 Structural properties of the catalysts used in this work

Property	1Rh/P25	1Rh/TSG	1Rh/NTSG	1Rh/NTSG-3Al_2O_3
Rh theoretical content, wt%	1	1	1	1
S_{BET}, m^2/g	55	155	260	182
Band gap energy Eg, support, eV	3.24	3.22	3.18	3.31
Band gap energy Eg, catalyst, eV	2.85	3.15	3.09	3.24
Valence band energy, eV	0.26	0.33	0.38	0.31
Conduction band energy, eV	−2.59	−2.82	−2.71	−2.93
Activation energy Ea, kJ/mol	65.6	153.4	116.7	101.3
Pre-exponential factor, 1/s	23.78	58.07	43.20	37.53
Rh particle size, nm	3.5	1.5	0.5	3.0
Rh surface density, atoms/nm^2	1.06	0.38	0.23	0.32
Dispersion, %	37	73	88	40
Rate, mol/g_{cat} s (at 50 °C)	0.36×10^{-4}	1.51×10^{-4}	4.35×10^{-4}	0.73×10^{-4}

of VOx species. They concluded that the structure and dispersion of VOx species depend on their surface density and on their interaction with a given support. Furthermore, the position of the absorption edge for low-energy charge transfer transitions has been shown to correlate with the domain size of the semiconductors and insulators [27]. In fact, the energy at the absorption edge has been used to characterize the size of MoOx, WOx, and VOx domains in catalytic solids [24, 27–30]. In our case, the energy at the absorption edge correlates with the dispersion and the particle size for the catalysts synthesized in this work.

The catalytic stability as a function of time for the three catalysts used in this work is reported in Fig. 2. At constant temperature, 100 °C, we found that CO conversion reaches 100%, but after 2 h there is already deactivation. The CO conversion falls up to 90% on 1Rh/NTSG, 92.5% on 1Rh/TSG, and 94% on 1Rh/NTSG-3Al_2O_3 catalysts after 16 h of reaction.

Nanotubes (NTSG) and nanoparticles (TSG) show a similar pattern of deactivation process during the first 6 h. After this time (6 h), nanotubes present a higher deactivation rate respect to the nanoparticles. The addition of 3 wt% of alumina to the nanotubes, however, seems to stabilize the structure of the nanotubes, hence the 1Rh/NTSG-3Al_2O_3 catalyst is less prone to the deactivation process compared to the nanotubes and nanoparticles surface for the CO oxidation. An explanation can be set forth, as the particle size

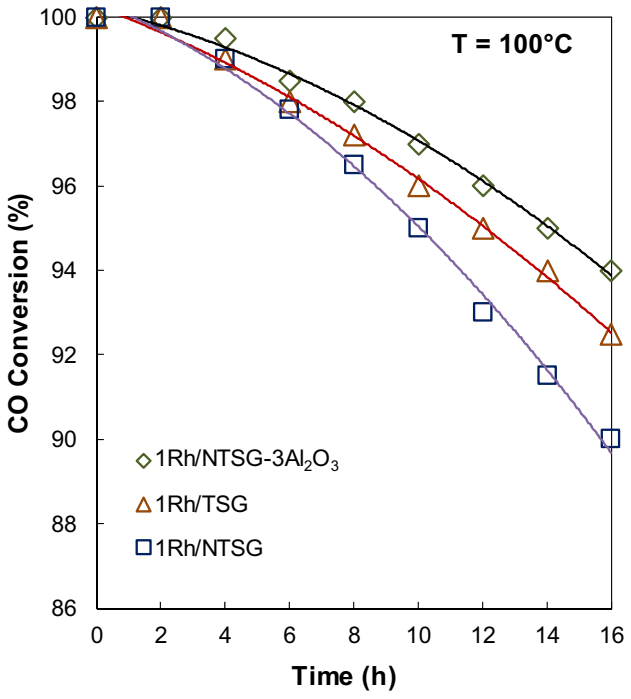

Fig. 2 Stability of the catalytic activity of the catalysts during CO oxidation as a function of time at 100 °C. 1 vol.% of CO, 1 vol.% of O_2, 50 mg of catalyst, and total flow of 100 mL/min

of Rh, reported in Table 1, supported on NTSG-3Al_2O_3 is around 3 nm, almost two-fold with respect to the particle size (1.58 nm) of Rh supported on TSG and six-fold respect to that supported on NTSG (0.5 nm). There is an apparent correlation between the deactivation process and the particle size of Rh. As the particle size of Rh increases the deactivation process is hindered.

Deactivation is a complex phenomenon that can be caused by poisoning, fouling, thermal degradation (evaporation, sintering), mechanical damage, and corrosion [31–33]. Other mechanisms of deactivation include masking and loss of the active elements [33]. The activity of a deactivating catalyst can be expressed according to the following equation:

$$a = r/r_0 \tag{3}$$

where r_0 is the initial rate of reaction, and r represents the rate of reaction measured after a determined time, a is the activity. Change of catalyst activity with time on stream is described by the following equation [33]:

$$-\frac{da}{dt} = k_d(a - a_{ss})^d \tag{4}$$

where a_{ss} is the steady-state activity reached at infinite time, d is the order of deactivation with respect to the driving force (a - a_{ss}). The general power-low Eq. (4) describes the kinetics of sintering by applying deactivation rate order 1 or 2 [33]. For $d=1$, it is suggested [34] that there is a parallel deactivation with no pore diffusion resistance to the reactant responsible for deactivation, oxygen in our case. In this sense, the integrated form of Eq. (4) for the case of $d=1$ is given by

$$a = a_{ss} + (1 - a_{ss})e^{(-k_d t)} \tag{5}$$

Besides,

$$F_{As} = F_{A0} - a(-r_{As})w \tag{6}$$

$$X_{as} = \frac{F_{A0} - F_{As}}{F_{A0}} \tag{7}$$

$$X_{As} = a_{ss} + (1 - a_{ss})e^{(-k_d t)}\left[\frac{(-r_{as})w}{F_{A0}}\right] \tag{8}$$

where F_{A0} is the initial molar flow rate (mol/h), w is the weight of the catalyst, g. X_{As} is the CO conversion at steady-state, %. The best fit was obtained for deactivation rate order d for a value of 1. Results are reported on Fig. 3. There is a satisfactory agreement between experimentally obtained and calculated CO conversion values for the three catalysts in Fig. 3.

Konova et al. [35] reported that the capacity of CO adsorption and the formation-accumulation of carbonates, as well as the agglomeration of Au particles after heating on the surface of the TiO_2 are the main causes involved in

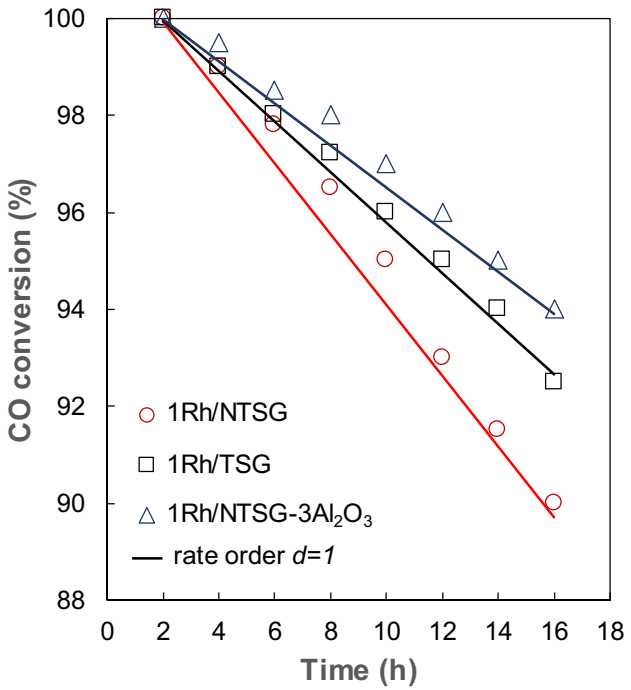

Fig. 3 Model validity test. Experimental and calculated values according to Eq. (8) for CO conversion as a function of time of reaction at 100 °C

the deactivation process. However, in our case, the possible formation of carbonates and the agglomeration of Rh particles on the surface of the support, as well as the changes in chemical composition and structure on the surface or bulk of the catalyst are investigated in the following sections.

3.2 Characterization by HR-TEM

The morphology of the catalysts 1Rh/P25, 1Rh/TSG, 1Rh/NTSG, and 1Rh/NTSG-3Al_2O_3 obtained by HR-TEM is reported in Fig. 4. Figure 4a shows that the particle size of TiO_2 (P25) was around 23 nm, and the particle size of Rh was, in average, 3.5 nm. The particle size of the TSG support on average is around 8 nm, and the particle size of Rh was around 1.5 nm, as reported in Fig. 4b. In the case of titanate nanotubes (NTSG), Fig. 4c shows that they presented an open-end tubular structure with external and internal diameters of 10 and 3.5 nm, respectively. The addition of 3 wt% of Al_2O_3, reported on Fig. 4d does not modify the structure of the nanotubes. Most of the nanotubes are open at both ends. Besides, each tube tends to have a constant diameter along its length. The presence of Rh on the surface of the supports was confirmed by EDS analysis (not showed). A summary of the morphology of the catalysts characterized by HR-TEM was included in Table 1.

3.3 Characterization by XRD

Figure 5 presents the characterization of the catalysts by XRD. We found, in Fig. 5a, that 1Rh/NTSG and 1Rh/NTSG-3Al_2O_3 catalysts display the monoclinic tri-titanic acid phase, $H_2Ti_3O_7$, with diffraction peaks at 2θ values of 9.7, 24, 28, 32.2, 48.4, and 50.0°, according to JCPDS file 36-0654. We also found in Fig. 5a that anatase is the main phase of the 1Rh/TSG catalyst, as indicated by the peaks located at 2θ values of 25.2° (101), 37.8° (004), 48.0° (200), 55.0° (211), 62.6° (204), and 75.0° (215), according to JCPDS file 21-1272. Further analysis by the Scherrer equation of the (101) diffraction peak at 2θ = 25.3° showed that the anatase crystal domains in the TSG catalyst measured about 8 nm.

In the case of the 1Rh/P25 catalyst, its diffraction pattern corresponds to a mixture of phases. It has a bi-crystalline structure composed of anatase and rutile phases. The primary size for the anatase crystals was estimated to be about 25 nm as measured from the X-ray line broadening technique using the Scherrer equation on the anatase 2θ = 25.3° (101) diffraction peak. The particle size of the rutile phase was about 35 nm on the rutile 2θ = 27.3° (110) diffraction peak.

To verify the structural stability, we measured the XRD pattern of the spent catalysts. Results are reported on Fig. 5b and show that 1Rh/NTSG and 1Rh/NTSG-3Al_2O_3 catalysts

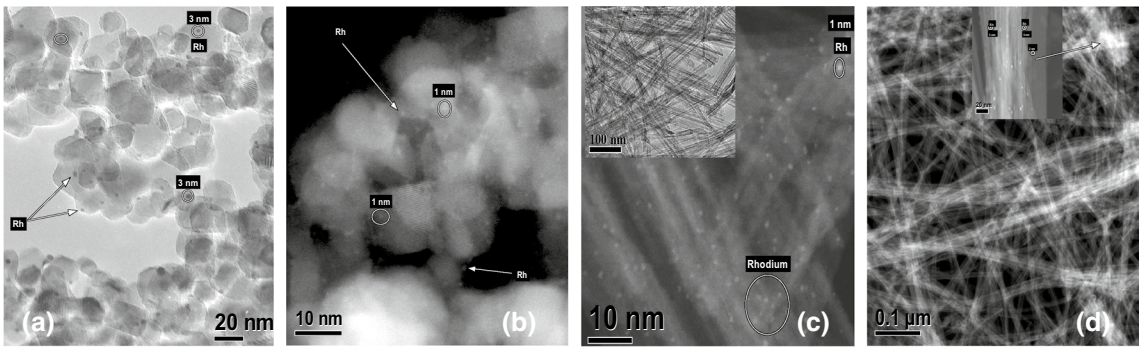

Fig. 4 HR-TEM micrographs for the catalysts used for CO oxidation. **a** 1/Rh/P25, **b** 1Rh/TSG, **c** 1Rh/NTSG, and **d** 1Rh/NTSG-3Al_2O_3

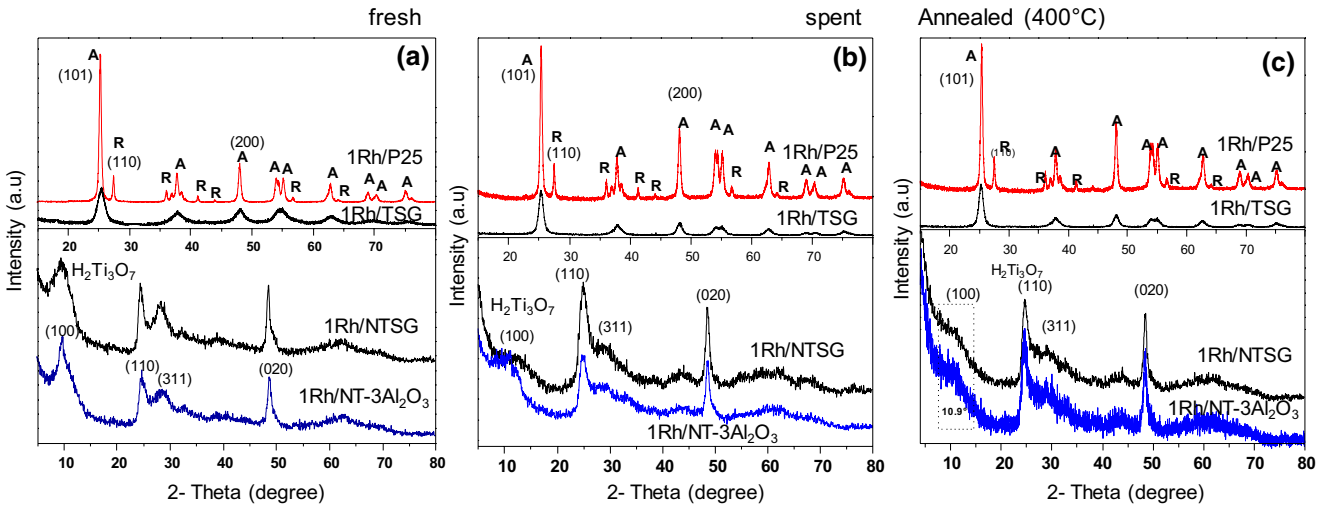

Fig. 5 XRD diffraction patterns for **a** fresh, **b** spent, and **c** annealed at 400 °C catalysts. A means anatase phase, R means Rutile phase, and $H_2Ti_3O_7$ is the tri-titanic acid phase

display changes principally in the peak located originally at 2θ = 9.7 (100). The (100) reflection shifts from 9.7° to 12.5° for 1Rh/NTSG and to 10.0° for 1Rh/NTSG-3Al_2O_3 catalyst. The corresponding initial ***d*** spacing for both catalysts for the 2θ angle located at 9.7° is 9.1 nm. For the 2θ angle shifted to 12.5°, i.e. for the 1Rh/NTSG catalyst, the corresponding ***d*** spacing is 7.0 nm. In the case of the 1Rh/NTSG-3Al_2O_3 catalyst, the corresponding ***d*** spacing shifted to 2θ = 10.0° is 8.8 nm.

The peak located around 2θ = 9.7° is attributed to the interlayer distance [36], and it has been reported [36, 37] that the shift towards larger angles may correspond to a decrease in the interlayer spacing in the titanate nanotube walls accompanied by removal of H_2O. In the case of the spent catalysts, this means that after 16 h at 100 °C, the structure of the support has been modified, and this could be part of the explanation for the loss in activity.

There is an apparent correlation between the spacing of the nanotube walls and the catalytic activity reported on Fig. 2. At 100 °C, CO conversion reached 100% on both catalysts (1Rh/NTSG and 1Rh/NTSG-3Al_2O_3). The initial spacing of the nanotube walls, for both catalysts, was 9.1 nm. After 16 h of reaction at 100 °C, CO conversion reached 90% with a *d* spacing of 7.0 nm on 1Rh/NTSG catalysts and 94% of CO conversion with a *d* spacing of 8.8 nm on 1Rh/NTSG-3Al_2O_3 catalyst. We can then suggest that as the spacing of the nanotube walls decreases, CO conversion diminishes. In the case of the 1Rh/NTSG-3Al_2O_3 catalyst, alumina probably acts as structure stabilizer of the nanotubes, as mentioned before.

In the case of the 1Rh/TSG and 1Rh/P25 catalysts, Fig. 5b shows that the support crystal size changes after 16 h of reaction at 100 °C. For 1Rh/TSG catalyst, the crystal size increased from 8 to 11 nm. In the case of 1Rh/P25 catalyst, the crystal size increased from 25 to 27 nm. Sintering of the support seems to be involved in the deactivation process reported in Fig. 2. As the TiO_2 crystal size increases during operation, the catalytic activity decreases.

Figure 5c shows the diffractograms for the samples annealed at 400 °C. For 1Rh/TSG, it is observed that the anatase structure is preserved. The anatase/rutile structures are observed for 1Rh/P25. However, 1Rh/NTSG and 1Rh/NT-3Al_2O_3 catalysts presented drastic changes. The release of physisorbed water occurs up to 110 °C on the support [38] and the thermal decomposition of $H_2Ti_3O_7$ is associated with a dehydration reaction taking place between 100 and 500 °C ($H_2Ti_3O_7 \rightarrow 3TiO_2 + H_2O$) [39]. The transformation of the nanotubes follows the sequence $H_2Ti_3O_7 \cdot xH_2O \rightarrow H_2Ti_3O_7 \rightarrow H_2Ti_6O_{13} \rightarrow Ti_2(B) \rightarrow TiO_2$ (anatase) between 140 and 500 °C [40]. In fact, nanotubes undergo complete dehydration at 500 °C, losing approximately 18% of their mass.

3.4 Characterization by H_2-TPR

Figure 6 shows the H_2-TPR profiles for 1Rh/TSG, 1Rh/P25, 1Rh/NTSG, and 1Rh/NTSG-3Al_2O_3 catalysts. In all cases the reduction of rhodium oxide species begins at low temperature, in agreement with a previous work [41]. All Rh species seem to be reduced at temperatures below 200 °C. Besides, TPR profile of the four catalysts suggests different degrees of strong metal-support interactions because of the variations in the wide reduction peak, extending from 25 °C to 175 °C depending on the sample studied. The second peak on the TPR profile, present with the nanotubes, extends between 270 and 500 °C and has been assigned to a partial

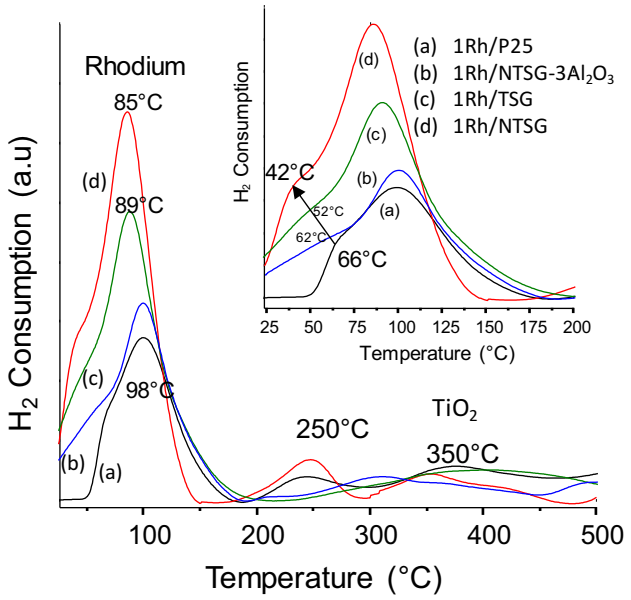

Fig. 6 H_2-TPR profiles for **a** 1Rh/P25, **b** 1Rh/NTSG-3Al_2O_3, **c** 1Rh/TSG, and **d** 1Rh/NTSG catalysts. The inset shows the H_2-TPR profiles for the four catalysts between 25 and 200 °C

reduction of the titanate nanotubes [42]. This region is not considered as important in our case, because our analysis was focused in the room temperature - 200 °C range, corresponding to the operating window of the catalytic tests.

1Rh/P25 reduction starts at 50 °C. It reaches a maximum at 98 °C and H_2 consumption finish at 180 °C. This catalyst (1Rh/P25) shows a low temperature shoulder located around 66 °C. Interestingly, the 1Rh/NTSG-3Al_2O_3 catalyst starts the reduction process at room temperature and the maximum is reached at 98 °C, following the behavior of the 1Rh/P25 catalyst. The shoulder shifted slightly from 66 to 62 °C. In the case of the 1Rh/TSG catalyst, we show in Fig. 6 that the maximum of the reduction peak was reached at 89 °C and the shoulder was shifted from 66 to 52 °C. A further temperature shift was observed for the 1Rh/NTSG catalyst. This catalyst reached the maximum at 85 °C and the shoulder was observed at 42 °C. These results indicate that the support has an important impact on the reduction process of our catalysts.

The correct parameter for comparison purposes during TPR process is the temperature-integrated H_2 consumption. The ratio of integrated H_2 consumption for 1Rh/NTSG-3Al_2O_3 to that of 1Rh/P25 was 1, i.e. H_2 consumption for both catalysts was essentially the same. However, in the case of the shoulder, the integrated-temperature H_2 consumption ratio was 3. This result means that H_2 consumption by the shoulder corresponding to 1Rh/NTSG-3Al_2O_3 was threefold than that of the 1Rh/P25 catalyst.

The integrated-temperature H_2 consumption ratio for the catalysts used in this work is presented in Table 2, with 1Rh/P25 catalyst used as a reference. Interestingly, for the 1Rh/NTSG-3Al_2O_3, 1Rh/TSG, and 1Rh/NTSG catalysts, we found, in Table 2, that H_2 consumption increased when compared to that for 1Rh/P25 catalyst. Furthermore, as the Rh particle size ratio decreases, the H_2 consumption ratio increases, and the shoulder reduction temperature of the catalysts was shifted to lower temperature, from 66 to 42 °C, as reported on Fig. 6.

It has been reported [43, 44] that the first peak is assigned to the reduction of Rh^{3+} (Rh_2O_3) to Rh^{1+} (Rh_2O), and the main peak is assigned to the reduction of Rh^{1+} to Rh^0. We suggest then that Rh^{3+} species plays an important role in the CO oxidation at low temperature. Furthermore, the Rh^{3+} species seems to be also involved in the shift to lower temperature of the CO oxidation, as reported on Fig. 1. However, the support has a strong influence on the Rh^{3+} species formation. In fact, the reduction of Rh^{+3} is improved by the supports as follows NTSG > TSG > NTSG-3Al_2O_3 > P25. In this line, we explore in the following section the Rh^{3+} species by XPS characterization of the catalysts.

The reaction that might take place during TPR is $Rh_2O_3 + 3H_2 \rightarrow 2Rh + 3H_2O$. In this sense, the stoichiometric amount of H_2 to reduce Rh is 3 mol H_2/mol of Rh_2O_3, or H_2/Rh = 1.50. Table 3 presents the amount of hydrogen consumed by the catalysts during TPR experiments. The amount of hydrogen consumed during TPR experiments is slightly higher than stoichiometric requirements for 1Rh/P25 and 1Rh/NTSG-3Al_2O_3 catalysts. In this case, hydrogen reduces Rh_2O_3 to Rh^0. For the 1Rh/TSG and 1Rh/NTSG catalysts, the hydrogen consumed is higher than stoichiometric, indicating that these peaks cannot be attributed only to the reduction of Rh_2O_3 to Rh^0. In fact, a possible contribution of TiOx reduction at low temperature may be occurring in the 1Rh/NTG and 1Rh/NTSG catalysts.

Table 2 Integrated-temperature H_2 consumption ratio

Catalyst-to-1Rh/P25 ratio	Total integrated-temperature H_2 consumption ratio	Integrated-temperature H_2 consumption ratio at shoulder	Rh particle size ratio
1Rh/NTSG-3Al_2O_3-to-1Rh/P25	1.00	3.00	0.85
1Rh/TSG-to-1Rh/P25	1.51	3.60	0.42
1Rh/NTSG-to-1Rh/P25	2.20	4.35	0.14

Table 3 TPR-H_2 consumptions for 1Rh-supported catalysts up to 175 °C

Catalyst	Total H_2 consumption (μmol H_2/g cat)	Peak I (μmol H_2/g cat)	Peak II (μmol H_2/g cat)	Total H_2/Rh ratio
1Rh/P25	168	8	160	1.12
1Rh/NTSG-3Al_2O_3	159	10	149	1.06
1Rh/TSG	202	11	191	1.34
1Rh/NTSG	281	28	253	1.87

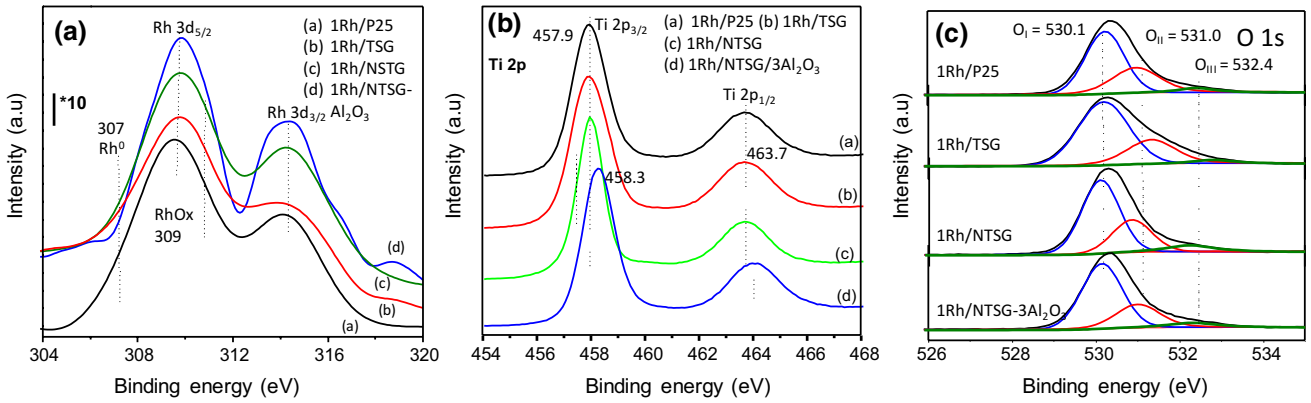

Fig. 7 XPS of **a** Rh 3d core level spectra, **b** Ti 2p core level spectra, and **c** O 1 s core level spectra for 1Rh/P25, 1Rh/TSG, 1Rh/NTSG, and 1Rh/NTSG-3Al_2O_3 catalysts

3.5 XPS Characterization

Figure 7 presents the XPS characterization of the catalysts used for CO oxidation in this work. Figure 7a presents the Rh3d core level spectra of the catalysts. It consists of a peak with maximum around 309.8 eV with a satellite located at 315 eV. These peaks correspond to an Rh^{3+} valence state. The result confirms the formation of Rh_2O_3 during impregnation on the different supports.

After reduction, Rh particles from the 1Rh/NTSG (309.8 eV) and 1Rh/NTSG-3Al_2O_3 (309.8 eV) catalysts have a larger value (+0.3 eV) of Rhd5/2 binding energy (BE) than those in 1Rh/P25 (309.5 eV) and +0.1 eV of Rhd5/2 BE when compared to 1Rh/TSG (309.7 eV). The increase of the BE by +0.3 eV in the case of the 1Rh/NTSG and 1Rh/TSG catalysts may indicate that rhodium particles are electron deficient [45].

This indicates that Rh particles in 1Rh/NTSG (0.5 nm), 1Rh/TSG (1.5 nm), and 1Rh/NTSG-3Al_2O_3 (3.0 nm) catalysts have a small positive charge ($Rh^{\delta+}$) compared to 1Rh/P25 (3.5 nm) catalyst, i.e. Rh on titanate nanotubes has a stronger interaction than with P25. By deconvolution of the Rh3d core level spectra, we found that there is a peak with binding energy of Rhd5/2 about 307 eV, which is attributed to Rh^0 metal (not shown). The Rh^{3+}-to-Rh^0 ratio of our catalysts is presented in Table 4. The relative concentration of Rh^{3+} species was around 70%. However, there is not a clear correlation between Rh^{3+}/Rh^0 ratio and the catalytic activity.

Table 4 XPS analysis for Rh3d and Ti2p core level of our catalysts

Catalyst	Rh^{3+}/Rh^0 ratio	Rh^{3+}/Ti^{4+} ratio	Rh^0/Ti^{4+} ratio
1Rh/P25	2.84	0.77	0.27
1Rh/NTSG-3Al_2O_3	2.57	0.77	0.29
1Rh/TSG	2.22	0.73	0.32
1Rh/NTSG	2.33	0.77	0.33

In addition to the Rh3d core level, Fig. 7b shows the Ti 2p XPS spectra for the catalysts reported in this study. We found that 1Rh/P25 catalyst presents a peak around 458.3 eV with a satellite around 464 eV. This suggests a 4^+ oxidation state for Ti in this catalyst. However, the other catalysts show a peak located at 457.9 eV. This value is close to that assigned for Ti^{3+} [45]. It seems that a partial reduction of the support through the Rh nanoparticles took place. It is possible that the strong metal support interaction promotes the formation of partially reducible oxide compounds like Rh^{3+}-TiO_{2-x}, in agreement with Sheerin et al. [46]. However, the Rh^{3+}/Ti^{4+} ratio, reported in Table 4, does not correlate with the catalytic activity.

A further analysis of the Ti2p and Rh3d spectra, for Ti^{4+} and Rh^0, showed that there is a possible correlation among these species (Ti^{4+} and Rh^0) and the catalytic activity,

however. In fact, Table 4 shows that Rh^0/Ti^{4+} ratio is promoted on NTSG support followed by TSG, NTSG-Al_2O_3, and P25, in agreement with results obtained by H_2-TPR, reported on Fig. 6. Furthermore, the Rh^0/Ti^{4+} ratio also correlates with the catalytic activity reported on Fig. 1.

We found that, as the Rh^0/Ti^{4+} ratio increases, the reduction temperature shifts to lower temperature, the catalytic activity improves, and the temperature for CO oxidation also shifts to lower temperature. Furthermore, the energy of the valence band of the catalysts seems to be also involved. We found that as the Rh^0/Ti^{4+} ratio increases, the valence band energy of our catalysts, reported in Table 1, also increases. This result implies that titania nanotubes (NTSG support) with a $H_2Ti_3O_7$ phase facilitate Rh^{3+} reduction to Rh^0, when compared to Rh supported on nanoparticles of TiO_2 with anatase structure (TSG support) or anatase–rutile phase (P25 support). However, addition of Al_2O_3 to nanotubes hinders the reducibility of Rh, as observed on Fig. 6, for NTSG-3Al_2O_3 support, apparently because the Rh^0/Ti^{4+} interaction is restricted by alumina. The O1 s spectra are reported on Fig. 7c.

The O 1 s peaks were fitted into three peaks. The first peak, related to the lattice oxygen (denoted as O_I), is located between 529.8 and 530.4 eV. The second peak has been related with chemisorbed oxygen (labelled as O_{II}). It is located between 531.1 and 531.9 eV, and a third peak (described as O_{III}), located between 532.5 and 532.9 eV, is related to the H_2O or CO_3 bonds on the surface [47]. In our case, Fig. 7c, shows that O1 s spectra of our catalysts present a main peak located at 530.1 eV due to the oxide ions of the TiO_2. The other two types of oxygen are ascribed to Ti–O bonds in Ti_2O_3 at 531 eV, and hydroxyl groups, at 532.4 eV. In fact, the primary band located around 530 eV (labelled as O_I) represents the lattice oxygen bound to Rh_3O_2 and TiO_2 phases. The band located around 531 eV, assigned as O_{II} is attributed to chemisorbed oxygen peak. This band includes adsorbed oxygen, adsorbed water, hydroxyl, and carbonate species [21]. We found that the O_I/O_{II} ratio correlates with the catalytic performance of our catalysts. Table 5 presents XPS results for O_I/O_{II} ratio.

Table 5 XPS results for the O_I/O_{II} ratio

Catalyst	O_I (%)	O_{II} (%)	O_I/O_{II} ratio
1Rh/P25	62	31	2.00
1Rh/NTSG-3Al_2O_3	61	29	2.12
1Rh/TSG	65	29	2.27
1Rh/NTSG	68	27	2.56

3.6 DRIFTS Characterization

The DRIFTS study of the catalysts was performed after an in situ reduction treatment under a flow of H_2/He (50 mL/min) at 400 °C for 1 h. Results of DRIFTS at 50 and 100 °C are reported in Fig. 8. Figure 8a shows that after introduction of CO at 50 °C, a band located at 2103 cm^{-1} appears on 1Rh/NTSG, 1Rh/TSG, and 1Rh/NTSG-3Al_2O_3 catalysts. This band is attributed to the stretching mode of linear monocarbonyl CO adsorbed on Rh^0 [48]. We also found a band located at 2074 cm^{-1} that has been identified as a linearly adsorbed CO species on Rh crystallites [49]. However, in the case of 1Rh/P25 catalyst, the twin bands at 2120 and 2090 cm^{-1} are attributed to the symmetric and asymmetric carbonyl stretching frequencies of gem dicarbonyl on the isolated Rh^I sites [49]. The adsorption band located at 2006 cm^{-1} observed on Fig. 8a for the four catalysts corresponds to CO which is linearly adsorbed on $Rh^{\delta-}$ sites or in the bridge form on $Rh^{\delta+}$ sites [49]. As the $Rh^{\delta-}$ species were not detected by XPS, however, we suggest that the band located at 2006 cm^{-1} corresponds to CO linearly adsorbed in the bridge form on $Rh^{\delta+}$ species.

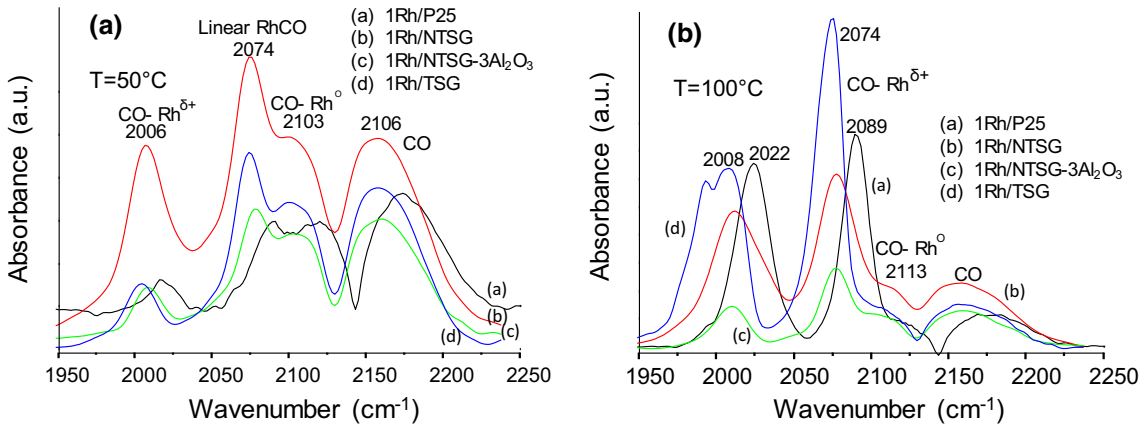

Fig. 8 FTIR-DRIFT spectra for CO adsorption at **a** 50 °C and **b** 100 °C on 1Rh/P25, 1Rh/NTSG, 1Rh/NTSG-3Al_2O_3, and 1Rh/TSG catalysts

The relative proportion of linear monocarbonyl CO adsorbed on Rh^0, linear adsorbed CO species on Rh crystallites, and the CO adsorbed in the bridge form on $Rh^{\delta+}$ sites on 1Rh/NTSG, 1Rh/TSG, and 1Rh/NTSG-3Al_2O_3 catalysts are reported on Table 6. Interestingly, the relative proportion of CO adsorbed species on Rh^0 (at 2074 cm^{-1}), and $Rh^{\delta+}$ (at 2006 cm^{-1}) sites, correlates with the catalytic activity reported on Fig. 1. In fact, 1Rh/NSTG catalyst promotes the adsorption of linear monocarbonyl CO on Rh^0 and the linear adsorbed CO species on Rh crystallites, followed by 1Rh/TSG, 1Rh/NTSG-3Al_2O_3, and 1Rh/P25 catalysts. CO adsorbed in the bridge form on $Rh^{\delta+}$ sites is preferred on 1Rh/TSG catalyst, followed by 1Rh/TSG, 1Rh/NTSG-3Al_2O_3 catalysts.

At 100 °C, Fig. 8b shows that the bands for CO adsorbed species on 1Rh/P25 at 2120 and 2090 cm^{-1} disappear. However, the bands corresponding to the adsorption of linear monocarbonyl CO on Rh^0 and the linear adsorbed CO species on Rh crystallites are enhanced. These results suggest that the linear adsorbed CO species on Rh^0 and Rh crystallites present a higher activity to oxidize CO when compared to CO adsorbed in the bridge form on $Rh^{\delta+}$ sites. Furthermore, the dicarbonyl CO adsorbed species on isolated Rh^I sites (on 1Rh/P25) are probably involved with a lower activity to oxidize CO respect to the other CO adsorbed species reported above.

Figure 9 presents DRIFTS spectra for the OH region at 3500-4000 cm^{-1} for 1Rh/TSG, 1Rh/P25, 1Rh/NTSG and 1Rh/NT-Al_2O_3 catalysts. The spectra of the four catalysts show the presence of an OH broad absorption band with two bands located at 3657 and 3715 cm^{-1}. Both bands correspond to OH groups, highly basic, at terminal positions due to stretching Ti–OH modes [50].

Table 7 presents the relative proportion of OH species adsorbed on the four catalysts for both bands reported on Fig. 9. In line with results obtained by CO adsorption (reported on Fig. 8), we found that the relative proportion of OH species absorbed at 3657 cm^{-1} is promoted on 1Rh/TSG catalyst, followed by 1Rh/TSG, 1Rh/NTSG-3Al_2O_3 catalysts. In fact, the relative proportion of OH species absorbed at 3657 cm^{-1} seems to correlate with the catalytic activity. As the relative proportion of OH species absorbed at 3657 cm^{-1} increases, the catalytic activity also increases.

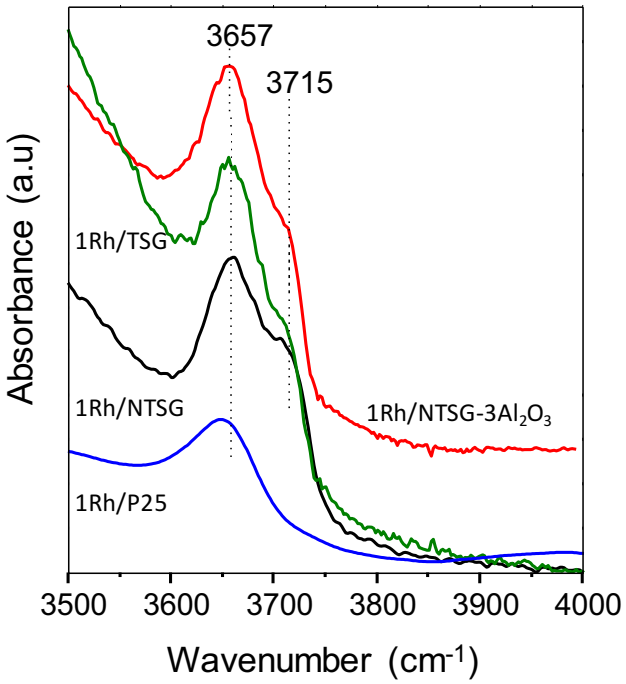

Fig. 9 FTIR-DRIFT spectra corresponding to hydroxyl species bands for the nanostructured catalysts

Furthermore, the Rh^0/Ti^{4+} ratio seems to promote the adsorption of OH species at 3657 cm^{-1}. We found that the amount of OH species increases along with the Rh^0/Ti^{4+} ratio. It is important to note on Fig. 9, however, that adsorption of OH species was completetlly blocked at 3715 cm^{-1} on 1Rh/P25 catalyst. These results suggest that OH groups absorbed at 3657 cm^{-1} on the surface of the catalysts are directly involved in the carbon monoxide oxidation on Rh-nanostructured catalysts. The OH species absorbed at 3715 cm^{-1} on the surface of the catalysts are probably involved with the shifts to lower temperature observed during CO oxidation and H_2-TPR test.

In this sense, it has been reported [51] that OH groups are important in the oxidation of CO because they contribute to the supply of active oxygen species and the regeneration of active sites during the carbon monoxide reaction. In fact, a moderate amount of OH species can promote low temperature CO oxidation on platinum-group-metal (PGM) catalysts [52]. In line with these observations, we confirm that OH

Table 6 Relative proportion of adsorbed CO species on Rh at 50 °C

Catalysts	2006 cm^{-1}	2074 cm^{-1}	2013 cm^{-1}	2120 to 2090 cm^{-1}
1Rh/P25	6.8			100
1Rh/NTSG-3Al_2O_3	12.8	23.8	17.9	
1Rh/TSG	19.6	28.1	42.8	
1Rh/NTSG	60.9	48.1	39.3	

Table 7 Relative proportion of OH species on Rh-supported catalysts

Catalysts	3657 cm^{-1}	3715 cm^{-1}
1Rh/P25	15.2	
1Rh/NTSG-3Al_2O_3	26.6	26.0
1Rh/TSG	27.3	26.6
1Rh/NTSG	29.2	47.4

species promotes the low temperature CO oxidation on Rh-nanostructured catalysts.

3.7 Redox Equilibrium

Lykaki et al. [21] in a paper about CO oxidation on Cu/CeO_2, propose that ceria (as support) promotes the formation of active oxygen species, whereas the copper-ceria interactions are involved in the formation of Cu^+ active species via the redox equilibrium $Ce^{4+} + Cu^+ \leftrightarrow Ce^{3+} + Cu^{2+}$. The proposed equilibrium is based on a Mars-van Krevelen redox type mechanism.

They suggest [21] that strong electronic perturbations result from the bonding interactions between metal nanoparticles and single atoms of support with great consequences in catalysis. However, as the size of the interacting particles increases the role of support is limited to the interfacial atoms [21].

In our case, CO_2 can be formed through the reduction of reducible species as Rh_2O_3 as follows:

$$Rh_2O_3 + 2CO \rightarrow Rh_2O + 2CO_2 \quad (9)$$

$$Rh_2O + CO \rightarrow 2Rh + CO_2 \quad (10)$$

Reactions (9) and (10) are supported by results obtained by FTIR-DRIFT (reported on Fig. 8). Regeneration of Rh^0 sites involves oxygen in gas phase as well as oxygen from the lattice of TiO_2.

$$2Rh + 2TiO_2 \leftrightarrow Rh_2O + Ti_2O_3 \quad (11)$$

$$4Rh + 3\,O_2 \rightarrow 2\,Rh_2O_3 \quad (12)$$

There is an apparent redox equilibrium between $Rh^0 + Ti^{4+}$ and $Rh^{\delta+} + Ti^{3+}$ ($\delta < 3$). However, the redox equilibrium Rh^0/Ti^{4+} seems to be modulated (limited) by the valence band energy of the catalysts, as observed in Fig. 10. The energy levels for the valence and conduction bands (reported in Table 1) were estimated from the XPS and UV–vis spectra, as reported by Ansari and Cho [26].

The Rh^0/Ti^{4+} ratio and the redox equilibrium between $Rh^0 + Ti^{4+}$ and $Rh^{\delta+} + Ti^{3+}$ ($\delta < 3$) are supported by the XPS results (reported on Fig. 7 and Table 4). We can then suggest that there is a clear electronic metal-support interaction effect (EMSI) that promotes the CO oxidation on Rh/TiO_2 catalysts. In fact, the Rhodium-TiO_2 interactions could be considered responsible for the formation of $Rh^{\delta+}$ active species via the redox equilibrium $Rh^0 + Ti^{4+} \leftrightarrow Rh^{\delta+} + Ti^{3+}$. However, the EMSI effect seems to be limited by the valence band energy of the catalysts.

The band gap is the energy difference between the highest occupied energy state of the valence band (the top of the valence band) and the lowest unoccupied state of the conduction band (the bottom of the conduction band) [53]. The band gap is the energy required to promote a valence electron bound to an atom to become a conduction electron. The valence band is the outermost electron orbital of an atom of a specific material that electrons occupy. In fact, the electrons located in the outermost shell of an atom are called valence electrons, they are involved in the chemical reactions and determine the electronic properties of the solid [53]. We suggest then that the valence band is a major factor determining the catalytic activity.

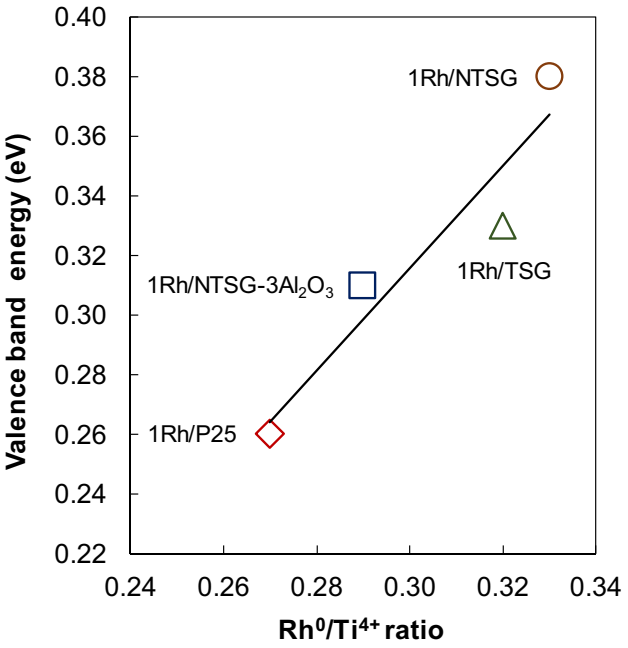

Fig. 10 Correlation between Rh^0/Ti^{4+} ratio and valence band energy of our catalysts as part of the equilibrium $Rh^0 + Ti^{4+}$ and $Rh^{\delta+} + Ti^{3+}$ ($\delta < 3$)

4 Conclusions

We investigated the CO oxidation on Rh-supported on nanoparticles and nanotubes of TiO_2. During light-off, we found that Rh supported on nanotubes presents the better catalytic activity compared to that supported on nanoparticles of TiO_2. At 70 °C, for instance, CO conversion was 93% on 1Rh/NTSG, 65% on 1Rh/TSG, 33% on 1Rh/NTSG-3Al_2O_3, and 10% on 1Rh/P25 catalysts.

Redox properties of the catalysts are involved in the performance of the catalytic activity. We found that, as the Rh^0/Ti^{4+} ratio increases, the reduction temperature of Rh shifts to lower temperature, the catalytic activity improves, and the temperature for CO oxidation also shifts to lower temperature. Furthermore, the energy of the valence band of the catalysts seems to be also involved. We found that as the Rh^0/Ti^{4+} ratio increases, the valence band energy of our catalysts also increases.

There is also an apparent redox equilibrium between $Rh^0 + Ti^{4+}$ and $Rh^{\delta+} + Ti^{3+}$ ($\delta < 3$). The redox equilibrium seems to be modulated (limited) by the valence band energy of the catalysts. Therefore, the valence band is a major factor determining the catalytic activity. We can conclude that electronic metal-support interactions (as a result from the contact between highly dispersed nanoparticles of Rh and nanotubes of TiO_2) facilitate the formation of the active $Rh^{\delta+}$ species via the redox equilibrium, hence the catalytic performance improves.

Acknowledgements Authors want to thank the financial support provided by the Mexican Institute of Petroleum via the Molecular Engineering Program (Project D.00477). RCS wishes to thank to the ICAT-UNAM and the financial support provided by the Consejo Nacional de Ciencia y Tecnología (CONACyT) through the PDNPN1216.

Compliance with Ethical Standards

Conflict of interest The authors declare no conflict of interest.

References

1. Cheng M, Zheng Y, Wan H (2013) Top Catal 56:1299
2. Su EC, Rothschild WG (1986) J Catal 99:506
3. Nibbelke RH, Nievergeld AJL, Hoebink JHBJ, Marin GB (1998) Appl Catal B 19:245
4. Shelef M, McCabe RW (2000) Catal Today 62:35
5. Bamwenda GR, Tsubota S, Nakamura T, Haruta M (1997) Catal Lett 44:83
6. Daté M, Haruta M (2001) J Catal 201:221
7. Chen MS, Cai Y, Yan Z, Gath KK, Axnanda S, Wayne D, Goodman W (2007) Surf Sci 601:5326
8. Zhu H, Qin Z, Shan W, Shen W, Wang J (2004) J Cat 225:267
9. Molina LM, Hammer B (2003) Rev Lett 90:206102
10. Valden M, Pak S, Lai X, Goodman DW (1998) Catal Lett 56:7
11. Lopez N, Janssens TVW, Clausen BS, Xu Y, Mavrikakis M, Bligaard T, Nørskøv JK (2004) J Catal 223:232
12. Joo SH, Park JY, Renzas JR, Butcher DR, Huang WY, Somorjai GA (2010) Nano Lett 10:2709
13. Ioannides T, Efstathiou AM, Zhang ZL, Verykios XE (1995) J Catal 156:265
14. Trautmann S, Baerns M (1994) J Catal 150:335
15. McClure SM, Goodman DW (2009) Chem Phys Lett 469:1
16. Tauster SJ, Fung SC, Garten RL (1978) J Am Chem Soc 100:170
17. Bavykin DV, Friedrich JM, Walsh FC (2006) Adv Mater 18:2807
18. Campbell CT (2012) Nat Chem 4:597
19. Hu P, Huang Z, Amghouz Z, Makke M, Hu F, Kapteijn F, Dikhtiarenko A, Chen Y, Gu X, Tang X (2014) Angew Chem Int Ed 53:3418
20. Konsolakis M (2016) Appl Catal B 198:49
21. Lykaki M, Pachatouridou E, Carabineiro SAC, Iliopoulou E, Andriopoulou C, Kallithrakas-Kontos N, Boghosian S, Konsolakis M (2018) Appl Catal B 230:18
22. Camposeco R, Castillo S, Mejía I, Mugica V, Carrera R, Montoya A, Morán-Pineda M, Navarrete J, Gómez R (2012) Catal Commun 17:81
23. Méndez-Cruz M, Ramirez-Solis J, Zanella R (2011) Catal Today 166:172
24. Chen K, Xie S, Iglesia E, Bell AT (2000) J Catal 189:421
25. López R, Gómez R (2012) J Sol-Gel Sci Technol 61:1
26. Ansari SA, Cho MH (2016) Sci Rep 6:25405
27. Khodakov A, Olthof B, Bell AT, Iglesia E (1999) J Catal 181:205
28. Khodakov A, Yang J, Su S, Iglesia E, Bell AT (1998) J Catal 177:343
29. Weber RS (1995) J Catal 151:470
30. Barton DG, Shtein M, Wilson RD, Soled SL, Iglesia E (1999) J Phys Chem 103:630
31. Forzatti P, Lietti L (1999) Catal Today 52:165
32. Bartholomew CH (2001) Appl Catal A 212:17
33. Fuentes GA (1985) Appl Catal 15:33
34. Levenspiel O (1979) Omnibook. Oregon State University, Corvallis
35. Konova P, Naydenov A, Venkov CV, Mehandjiev D, Andreeva D, Tabakova T (2004) J Mol Catal A 213:235
36. Bavykin DV, Carravetta M, Kulak AN, Walsh FC (2010) Chem Mater 22:2458
37. Chen Q, Du GH, Zhang S, Peng L (2002) Acta Cryst B58:587
38. Liu N, Chen J, Zhang J, Schwank JW (2014) Catal Today 225:34
39. Mosia S, Borowiak-Palén E, Przepiórski J, Grzmil B, Tsumura T, Toyoda M, Grzechuldka-Damszel J, Morawski AW (2010) J Phys Chem Solids 71:263
40. Mejía-Centeno I, Castillo S, Camposeco R, Marín J, García LA, Fuentes GA (2015) Chem Eng J 264:873
41. Ehwald H, Ewald H, Gutschick D, Hermann M, Miessner H, Ohlmann G, Schierhorn E (1991) Appl Catal 76:153
42. Wong C, McCabe RW (1987) J Catal 107:535
43. Shinmi Y, Koso S, Kubota T, Nakagawa Y, Tomishige K (2010) Appl Catal B 94:318
44. Camposeco R, Castillo S, Rodríguez-González V, Hinojosa-Reyes M, Mejía-Centeno I (2018) J Photochem Photobiol, A 356:92
45. Larichev YV, Netskina OV, Komova OV, Simagina VI (2010) Int J Hydrogen Energy 35:6501
46. Sheerin E, Reddy GK, Smirniotis P (2016) Catal Today 263:75
47. Wang C, Shao C, Zhang X, Liu Y (2009) Inorg Chem 48:7261
48. Guang H, Lin J, Li L, Wang X, Zhang T (2016) Appl Catal B 184:299
49. Zhang ZL, Kladi A, Verykios XE (1994) J Mol Catal 89:229
50. Hadjiivanov K, Lamotte J, Lavalley JC (1997) Langmuir 13:3374
51. Ramis G, Busca G, Lorenzelli V (1987) J Chem Soc. Faraday Trans 83:591
52. Lin J, Wang X, Zhang T (2016) Chin J Catal 37:1805
53. Gersten GI, Smith FW (2001) The Physics and Chemistry of Materials, 1st edn. Wiley, New York